Exit-channel recoil resonances by imaging the photodissociation of single quantum-state-selected OCS molecules

Dimitris Sofikitis,[1,2,*] Jaime Suarez,[3,†] Johan A. Schmidt,[4,5] T. Peter Rakitzis,[2,6]
Stavros C. Farantos,[2,7] and Maurice H. M. Janssen[1,‡]

[1]*LaserLaB, Department of Physics and Astronomy, VU University, De Boelelaan 1081, Amsterdam 1081 HV, The Netherlands*
[2]*Institute of Electronic Structure and Laser, Foundation for Research and Technology–Hellas, 71110 Heraklion-Crete, Greece*
[3]*Departamento de Qumica, Modulo 13, Universidad Autonoma de Madrid, Cantoblanco 28049, Madrid, Spain*
[4]*Department of Chemistry, University of Copenhagen, Universitetsparken 5, DK-2100 Copenhagen Ø, Denmark*
[5]*Airlabs, Ltd., Ole Maaloes Vej 3, Copenhagen, DK-2200, Denmark*
[6]*Department of Physics, University of Crete, 71003, Heraklion-Crete, Greece*
[7]*Department of Chemistry, University of Crete, 70013, Heraklion-Crete, Greece*

(Received 11 May 2018; published 26 September 2018)

In a recent letter [Phys. Rev. Lett. **118**, 253001 (2017)] we have described how studies of the recoil velocity distribution in the photodissociation of OCS in the energy interval 42 600–42 900 cm^{-1} revealed an unexpected behavior: the recoil velocity distribution of only the lowest-kinetic-energy photofragments exhibited rapid, resonantlike variations with energy and caused complete inversion of the recoil direction. Periodic orbit analysis and quantum nonadiabatic calculations unveiled the existence of a resonance state localized at large bending angles towards the exit of the dissociation channel. In this article, we present an extensive theoretical study and we show how the fingerprints of these resonances are identified by the analysis of the nonadiabatic transitions and the stereodynamics of photofragments trajectories. Additionally, the experimental study is extended to a second photolysis energy region, 43 300–43 650 cm^{-1}, where a similar rapid variation of the recoil direction is detected. The energy separation between this second resonance region and the one previously reported is ∼800 cm^{-1}, which is twice the calculated period of the localized resonant state, offering a second point of convergence between the experiment and the theory.

DOI: 10.1103/PhysRevA.98.033417

I. INTRODUCTION

Studying the photodissociation of small molecules elucidates the way in which energy is transferred in the various molecular degrees of freedom and can give valuable information for the construction of the potential energy surfaces (PESs) which govern the molecule's energetics [1]. This information provides the means to achieve control over elementary chemical processes, such as the coherent control of chemical reactions [2,3]. Furthermore, detailed experimental and theoretical studies of the photodissociation of small molecules like N_2O and OCS are of profound importance for modeling global atmospheric budgets and climate-regulating mechanisms [4,5]. Two climate-regulating mechanisms are intricately linked to OCS, despite the fact that it makes up only a tiny fraction of the Earth's atmosphere; thus the role of OCS is currently an active area of atmospheric research [6–8].

The stereodynamical aspects of photodissociation can be studied using a variety of modern spectroscopic techniques, such as ion imaging [9], velocity map imaging (VMI) [10,11], recoil-ion and electron momentum spectroscopy [12], or Rydberg tagging [13]. Such studies have demonstrated that the dissociation reactions, even in the case of small molecules, can be the result of complicated underlying mechanisms [14–17], such as the roaming mechanism [18–23] or the interference between multiple dissociating states [24–28].

The angular (spatial) distribution of the photofragments resulting from the simple, one-photon photodissociation of *nonoriented* molecules, and in the absence of any angular momentum polarization, is described by the well-known expression [29]

$$I(\theta) \propto 1 + \beta_2 P_2(\cos\theta), \tag{1}$$

where β_2 is the spatial anisotropy parameter, which ranges from –1 to 2, and P_n are the Legendre polynomials.

When photodissociation of laboratory-frame-oriented molecules is considered, more free parameters have to be used to describe photofragment spatial distribution, again through an expansion in Legendre polynomials [29–36]:

$$I(\theta) \propto 1 + \beta_1 P_1(\cos\theta) + \beta_2 P_2(\cos\theta) + \beta_3 P_3(\cos\theta) + \beta_4 P_4(\cos\theta). \tag{2}$$

The β_1 parameter is related to up-down asymmetries, the β_2 is related to parallel-perpendicular, and the β_3 and β_4 are related

*sofdim@iesl.forth.gr; info@massspecpecd.com
†Current address: Dipartimento di Chimica, Università degli Studi di Milano, 20133 Milano, Italy.
‡Current address: MassSpecpecD BV, High Tech Campus, University of Twente, Drienerbeeklaan, 35 7522NA Enschede, The Netherlands.

to high-order asymmetries. In the absence of orientation all terms except β_2 are zero.

In recent work [37], we have studied the photodissociation of laboratory-frame-oriented OCS molecules in the range 42 600–42 900 cm^{-1} and observed that more than 30 rotational states of carbon monoxide are produced. By dissociating single quantum-state-selected OCS ($v_2 = 1|J, l = 1, 1$), we have observed that the CO ($v = 0$) and S($^1D_2$) correlated photofragments associated with the $J_{CO} = 66$ rotational state, which is the highest rotational excitation and consequently the lowest-kinetic-energy state at this photolysis energy, recoil in the opposite direction with respect to the recoil direction, followed by the CO($v = 0;J$), S($^1D_2$) photofragments associated with all other states ($J_{CO} \leqslant 65$). With J we denote the total angular momentum, with l the projection of J on the linear symmetry axis. A closer examination reveals that the recoil direction of these fragments, described by the aforementioned β parameters, varies rapidly, in a resonant fashion, as a function of the photolysis energy, hereby referred to as a "recoil resonance." The "recoil resonance" affects only fragments of the lowest kinetic energy, which can be related to cold-molecule collisions and orbiting resonances, which in turn are related to (cold) association reactions in outer space or low-energy barrierless reactions [14,38–41].

In this article we present an experimental study and extended theoretical calculations and discussion of the phenomenon in terms of periodic orbit (PO) analysis and grid-based nonadiabatic quantum dynamical analysis. In the previous investigation [37], the emphasis was given in studying the inversion in the recoil direction of a single CO rovibrational state, coming from the dissociation of laboratory-frame-oriented parent OCS molecules; this recoil inversion is detected through the β_1 coefficient, which takes negative values. However, the fingerprints of the long-lived resonant state that uncovers the recoil inversion are also evident in the resonantlike variation of the β_2 parameters with energy that accompanies the phenomenon. Since extracting the β_2 parameters does not require laboratory-frame orientation, studying the resonant state dynamics through the variation of the β_2 parameters offers a solution which is less demanding from an experimental point of view.

We have recorded the recoil velocity distribution of several J_{CO} rotational states in the energy range of 42 600–42 900 cm^{-1} and show that only the recoil geometry of the lowest-kinetic-energy fragments exhibits a resonant behavior. This is a practical way to examine the photodissociation dynamics in the *presence* and in the *absence* of the resonant state; since only the fragments of minimum kinetic energy are affected by the subtleties of the molecular potential, we can minimize their effect on the dissociation dynamics by simply extending the study to CO states with reduced rotational excitation, and therefore increased kinetic energy.

Additionally, we extend the first experimental study [37] to a second energy region, namely, 43 300–43 650 cm^{-1}, where a similar "recoil resonance" is detected. This new resonance is found at an energy which is ~800 cm^{-1} higher than the one previously reported [37]. This difference is twice the vibrational period of the resonant state identified by the periodic orbit and quantum nonadiabatic analysis. The new "recoil resonance" is more diffused (expressed by a Beutler-Fano–type shape [42]), in accordance to the theoretical calculations, which demonstrates that the resonance states at higher energies show a stronger mixing of the discrete with the continuum part of the spectrum.

II. EXPERIMENTAL

A. Details

The experimental setup to measure the OCS photofragment distributions has been explained elsewhere [43]. Briefly, it consists of a hexapole, quantum state-selector which focuses OCS molecules in the $v_2 = 1$ vibrationally excited bending state, and the $|J, l\rangle = |1, 1\rangle$ state of the OCS molecules participating in a molecular beam, to the intersection volume of the photolysis and ionization lasers. The l angular momentum projection is generated by rovibrational angular momentum of the ν_2 degenerate bending modes.

The photolysis field is generated by frequency doubling of the output of an Nd-YAG pumped, pulsed dye laser. The polarization is linear and parallel to the orientation direction. The S($^1D_2$) atomic fragments are ionized using an additional nanosecond laser, set at frequency around 34 308 cm^{-1} via the $^1F_3$ sulfur line. When instead of the atomic S fragments the molecular CO fragments are detected, the ionization lasers are tuned to around 230 nm, depending on the J_{CO} rotational state to be probed [44]. The ionization laser is also linearly polarized parallel to the orientation axis of the OCS molecules, while the photolysis and ionization lasers counterpropagate. Both the photolysis and ionization lasers have a pulse duration of ~6 ns and a bandwidth close to 0.5 cm^{-1}. After dissociation, additional electric fields are actuated to focus the ions to a two-dimensional position-sensitive detector using the VMI technique [10,43].

B. Results

The photodissociation of carbonyl sulfide has experimentally been studied by VMI and hexapole quantum state selector techniques in a range of energies of 42 300–43 650 cm^{-1}. A detailed analysis was carried out for photolysis energies around 42 700 cm^{-1} with laboratory-frame-oriented parent molecules in [37], whereas here, the study is extended to photolysis energies around 43 500 cm^{-1} using nonoriented molecules. The β_2 anisotropic parameter, which characterizes the angular (spatial) distribution of the photofragments, was extracted from the experimental measurements and revealed resonantlike variations only for the lowest-kinetic-energy photofragments, and thus, for the highest J_{CO} states.

Specifically, for an energy of 42 700 cm^{-1} we observed for photolysis of laboratory-frame-oriented OCS a resonance, which brings the sulfur atom closer to the oxygen rather than the carbon atom [37]. This resonant state is associated with high-angular-momentum product CO states.

In these photolysis energies, the CO fragments are generated in the ground vibrational state [25,45] and in more than 30 rotational states. In Fig. 1 we see the sliced ion images corresponding to five different values of CO rotational angular momentum, $J_{CO} = 61$, 62, 63, 64, and 65, which correspond to a photodissociation energy of 42 607.6 cm^{-1}

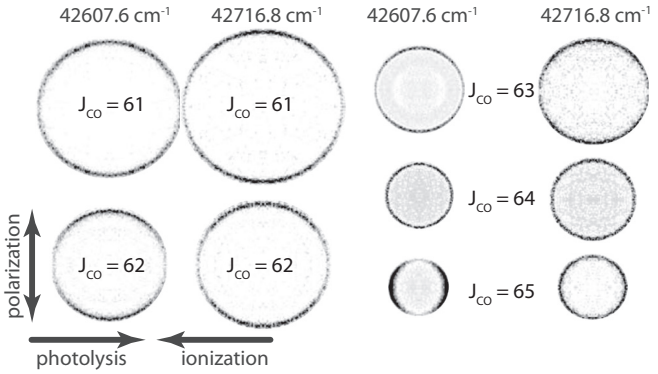

FIG. 1. Characteristic symmetrized sliced ion images of CO ions resulting from the photodissociation in two different wavelengths, $E_{\text{diss}} = 42\,607.6$ nm and $E_{\text{diss}} = 42\,716.8$ nm. The CO states detected are $J_{\text{CO}} = 61$, 62, 63, 64 and 65, while ions which correspond to different rotational numbers have been cropped out. The horizontal arrows mark the propagation directions of the photolysis and ionization lasers, respectively, while the vertical arrow marks their polarizations.

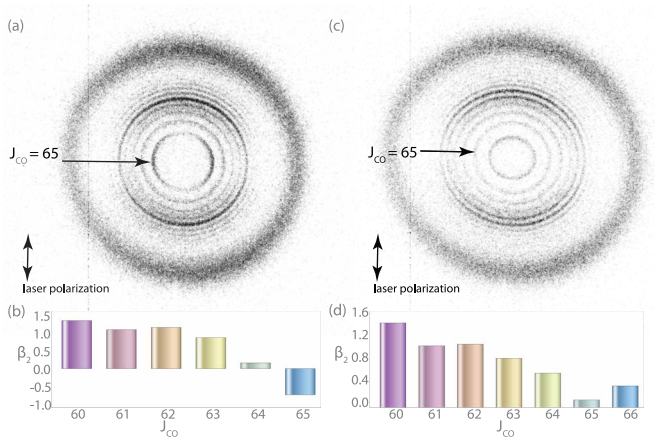

FIG. 2. (a) Sliced ion image of sulfur ions produced by dissociation of OCS with a photolysis laser energy of 42 594.14 cm^{-1}. (b) The β_2 parameters extracted from the figure shown in (a). (c) Sliced ion image of sulfur ions produced by dissociation of OCS with a photolysis laser energy of 42 719.83 cm^{-1}. (d) The β_2 parameters extracted from the figure shown in (c).

($\lambda_{\text{diss}} = 234.74$ nm) and to a slightly larger photodissociation energy of 42 716.8 cm^{-1} ($\lambda_{\text{diss}} = 234.1$ nm).

For these velocity-mapped images, the diameter of the ion sphere is proportional to the fragment's kinetic energy after dissociation. For the rotationally highly excited J_{CO}, the kinetic energy is reduced, since a large part of the photolysis energy is converted to rotational energy. As we see in the figure, the higher kinetic energy fragments, namely, $J_{\text{CO}} = 61$ and 62, are preferentially emitted to a direction parallel to the photolysis polarization direction. As the kinetic energy of CO(J) fragments is reduced with increasing rotational state for $J_{\text{CO}} = 63$, 64, and 65, the angular recoil velocity distribution becomes more isotropic.

In all these cases, the velocity distribution of the fragments produced by dissociation at $\lambda_{\text{diss}} = 234.7$ nm and $\lambda_{\text{diss}} = 234.1$ nm is similar, with the exception of the lowest kinetic energy fragments, correlated to the highest J_{CO} values. The $J_{\text{CO}} = 65$ photofragments produced using a photolysis wavelength of $\lambda_{\text{diss}} = 234.1$ nm are emitted isotropically. In contrast, the velocity distribution of the $J_{\text{CO}} = 65$ photofragments at $\lambda_{\text{diss}} = 234.7$ nm are emitted preferentially perpendicularly to the polarization of the photolysis laser.

It is thus reasonable to ask how would the recoil direction change for photofragments of different kinetic energy at various nearby photolysis energies. An improved method for achieving this objective is to employ an indirect detection of the various J_{CO} rotational states by probing the correlated S($^1D_2$) cofragment. In Fig. 2(a) we see a characteristic sliced ion image of the sulfur ions created after photodissociating $|J, l\rangle = |1, 1\rangle$ OCS molecules at a photolysis energy of $\sim$42 600 cm^{-1}. We see that the image contains several distinct velocity groups. Each group corresponds to the production of CO fragments in a different rotational state J_{CO}. For the focusing conditions chosen here, the following J_{CO} states are resolved: From inner to outer, the rings correspond to $J_{\text{CO}} =$ 65, 64, 63, 62, 61 (brighter ring) and 60. The broad ring is formed by ions corresponding to $34 \leqslant J_{\text{CO}} \leqslant 54$ (unresolved). Thus, by detecting the sulfur ions one can study the correlated angular distribution of the recoil velocity for multiple J_{CO} rotational states in a single image.

The value of the β_2 parameter can range from values close to +2 to values close to –1 [30]. When linear polarization of the photolysis is considered (as is the case here), values close to +2 correspond to recoil parallel to the photolysis polarization. Values close to –1 correspond to recoil perpendicular to the photolysis polarization. Finally, values close to zero describe nearly isotropic velocity distributions.

In Fig. 2(b), we see the values of β_2 corresponding to the ion image shown in Fig. 2(a). In Fig. 2(c) we see a similar ion image produced in the photodissociation energy $\sim$42 719 cm^{-1}, while Fig. 2(d) shows the β_2 values extracted from the image shown in Fig. 2(c). We can analyze the dynamics of the system by comparing the values of the β_2 parameters for the two wavelengths.

As we see, for the lower values of J_{CO}, which correspond to higher kinetic energy, the velocity distributions are similar, and the corresponding β_2 parameters are large and positive (albeit larger in the case of photolysis energy 42 700 cm^{-1}). For the case of the lower-kinetic-energy photofragments, the differences in recoil velocity distributions are much larger, while in the case of photolysis energy 42 600 cm^{-1} [Figs. 2(a) and 2(b)], the lowest-kinetic-energy fragments associated with $J_{\text{CO}} = 65$ recoil perpendicularly to the photolysis polarization (negative β_2). For a photolysis energy $\sim$100 cm^{-1} larger, this does not happen and the values of β_2 for the $J_{\text{CO}} = 65$ ions are close to zero, corresponding to nearly isotropic velocity distributions. (Note that for this photolysis energy, an additional rotational state, namely, the $J_{\text{CO}} = 66$, has appeared.) In all the studies mentioned, the β_4 coefficients are within error of zero, suggesting negligible contribution of any polarization effects.

In order to extract a more complete picture of the dynamics, we have repeated this study for various photolysis

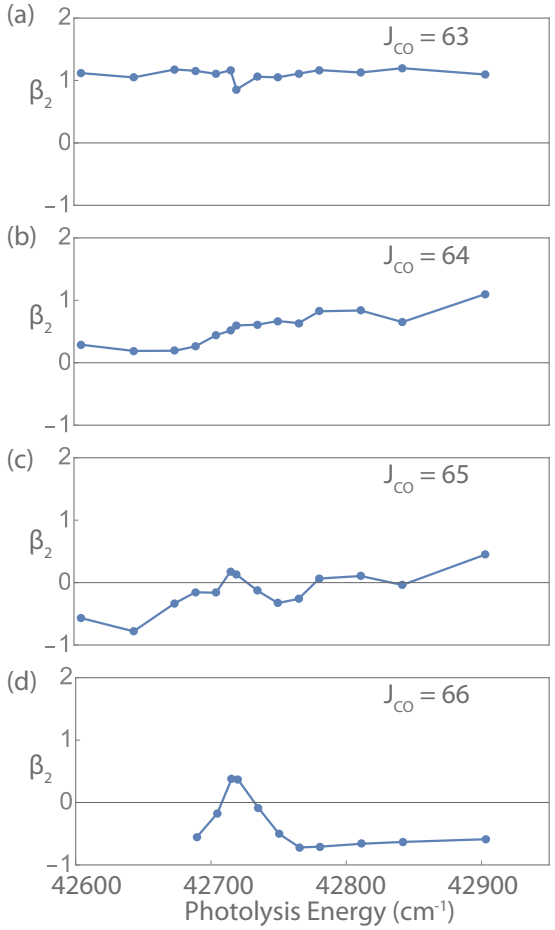

FIG. 3. Evolution of the β_2 parameter with respect to the photolysis energy around 42 700 cm^{-1}. Panel (d) has been adapted from Ref. [37].

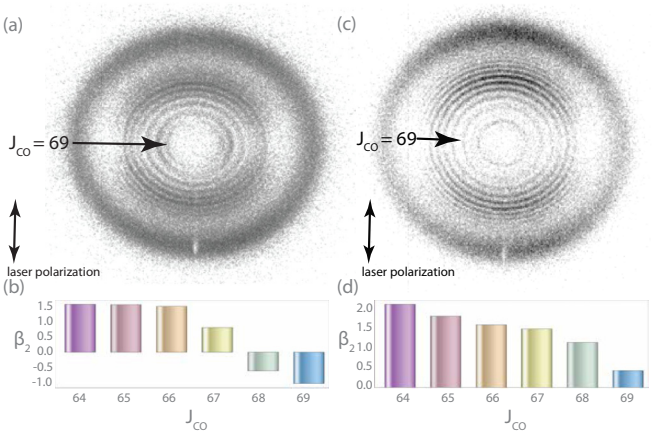

FIG. 4. (a) Sliced ion image of sulfur ions produced by dissociation of OCS with a photolysis laser energy of 43 434.6 cm^{-1}. (b) The β_2 parameters extracted from the figure shown in (a). (c) Sliced ion image of sulfur ions produced by dissociation of OCS with a photolysis laser energy of 43 497.6 cm^{-1}. (d) The β_2 parameters extracted from the figure shown in (c).

energies, ranging from 42 600 to 42 950 cm^{-1}, with the results shown in Fig. 3. As we see, the lowest-kinetic-energy fragments, corresponding to $J_{CO} = 66$, show a rapid, resonantlike variation of the β_2 parameter: its value is negative for energies $\sim$42 680 cm^{-1}. For a small range of energies $42\,690 \leqslant E_{diss} \leqslant 42\,750$ cm^{-1} (hereby denoted as recoil resonance area), β_2 switches sign and as the photolysis energy increases, β_2 switches sign again and remains negative for energies as high as 42 900 cm^{-1}.

The ions correlated to the $J_{CO} = 65$ rotational state also show variations of the β_2 parameter with increasing photolysis energy, although not as large as for $J_{CO} = 66$. The β_2 values are negative in the low end of the photolysis energy spectrum and gradually increase and take positive values, albeit close to zero, in the high end of the photolysis spectrum. For the next CO rotational state $J_{CO} = 64$, the β_2 parameter shows a slow variation from positive values close to zero at the low end of the spectrum towards larger values close to one at the high end. As J_{CO} decreases, the values of the β_2 parameter approach unity and their variation with respect to the photolysis energy becomes smaller.

Since the rotational constant for the ground $X^1\Sigma^+$ state of the CO molecule is 1.93 cm^{-1} [46], the energetic distance between the highest $J_{CO} = 66$ rotationally excited state and the $J_{CO} = 63$ state is $\sim$750 cm^{-1}, which is well above the height of the local minimum of the X-PES, which is close to 250 cm^{-1}. Thus, it is safe to assume that the dynamics of the lowest rotational excitation state $J_{CO} = 63$ shown here will not reflect the effects of the resonant state and will be more representative of the conventional dissociation dynamics for this molecular system. Note that the β_2 parameter of the $J_{CO} = 63$ state has a constant value for photolysis energies over the 42 600–42 900 cm^{-1} interval.

Note that these resonancelike, rapid variations in the recoil direction are not accompanied by any modification in the $J_{CO} = 66$ product state population [37], nor by any (important) variation of the total cross section [47]. This is consistent with previous studies which reveal a uniform distribution of the probability for production of S(^1D) atoms, contrary to the production of S(^3P) atoms, which is characterized by resonant features [48].

As presented in the theory section, the rapid modification of the recoil velocity directions are attributed to resonances with neighboring eigenenergy differences of $\sim$400 cm^{-1}. We have repeated the study of the evolution of the β_2 parameter with respect to energy for a photolysis energy close to 43 500 cm^{-1}, i.e., two vibrational periods away from the resonance reported in [37]. In this photolysis energy region, an additional, yet more diffused resonance is identified by the theoretical calculations.

In Fig. 4(a) we show a characteristic sliced ion image of sulfur atoms produced at a photolysis energy of 43 434.6 cm^{-1}. Here, the lowest-kinetic-energy photofragments are associated with the $J_{CO} = 69$ rotational state, and we see that these ions are preferentially emitted in a direction perpendicular to the polarization of the photolysis laser, as well as the ions associated with the next $J_{CO} = 68$ rotational state. The values of the β_2 parameter for the various J_{CO} states are shown in Fig. 4(b). In Fig. 4(c) we show a sliced ion image for a photolysis energy of 43 497.6 cm^{-1}, while in Fig. 4(d) we show the β_2 parameters extracted from this

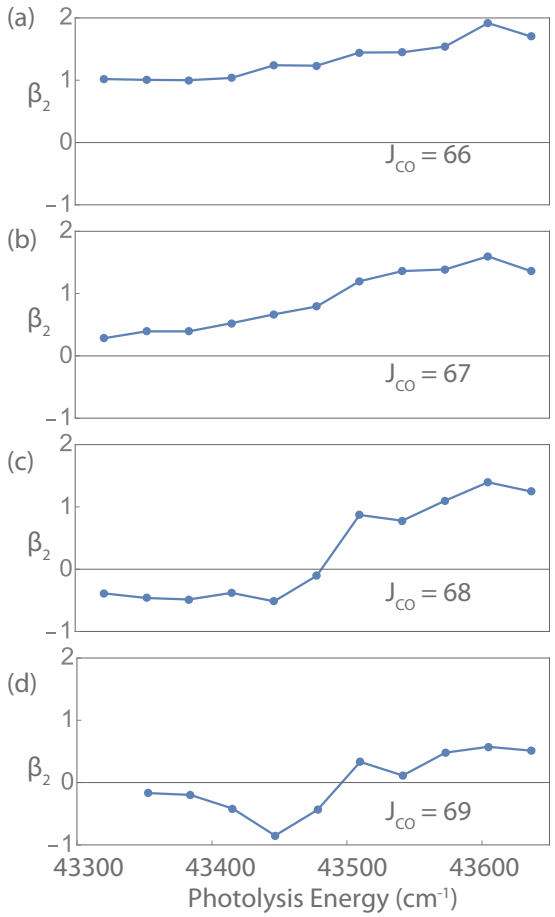

FIG. 5. Evolution of the β_2 parameter with respect to the photolysis energy around 43 500 cm^{-1}.

image. We see that by increasing the photolysis energy by ~60 cm^{-1}, the recoil geometry changes dramatically, since the ions associated with the rotational states $J_{CO} = 69$ are now isotropically emitted. Note that the photolysis energy increase is enough so that an additional rotational state is now produced.

In Figs. 5(a)–5(d) we see the β_2 parameters of the states for $66 \leqslant J_{CO} \leqslant 69$ as a function of photolysis energy. Again, for the J_{CO} state that is closest to threshold, where $J_{CO} = 69$ [Fig. 5(d)], there is a variation of the β_2 parameter, however, not as sharp as the one depicted in Fig. 3(d). A similar variation, albeit of smaller amplitude, is found in the evolution of the β_2 parameter of the $J_{CO} = 68$ photofragments, shown in Fig. 5(c).

The evolution of the β_2 parameter with respect to the photolysis energy becomes even more smooth as the kinetic energy of the fragments increases (and thus, the rotational excitation decreases) to the point that by the time the rotational excitation reaches $J_{CO} = 66$, no resonant features are present but rather the β_2 parameter gradually increases from values near unity to values near 2. Again, the lowest rotational state, here $J_{CO} = 66$, has a kinetic energy higher by ~780 cm^{-1} with respect to the "near-threshold" state $J_{CO} = 69$, and we can assume that the photodissociation dynamics for the $J_{CO} = 66$ state will not be affected by the shallow local minimum of the X-PES, similar to the $J_{CO} = 63$ state in the previous photolysis energies around 42 700 cm^{-1}. However, for the $J_{CO} = 66$ state around 43 500 cm^{-1}, the evolution of the β_2 parameter is not constant with respect to the photolysis energy but rather a smooth increase that changes β_2 by a one within 300 cm^{-1}. This smooth increase seems to be present also in the evolution of the β_2 parameter of the higher excited state with $J_{CO} = 67$, 68, and 69. The simultaneous presence of both a resonant feature and a slowly varying background in these states might be responsible for the dispersive shape of the β_2 spectrum and calls for further examination.

III. NUMERICAL CALCULATIONS

A. Adiabatic potential energy surfaces

The three-dimensional potential energy surfaces, which are mainly involved in the dissociation process of OCS, in the range of photodissociation energies under consideration (42 600–43 600 cm^{-1}), correspond to the X and A electronic states. Analytical potential functions were constructed via three-dimensional spline interpolation from electronic-structure calculations in C_s symmetry for the two lowest A' adiabatic states. The method of multiconfiguration reference internally contracted configuration interaction (MRCI) was employed with wave functions obtained by state-averaged full-valence complete active space self consistent field (CASSCF) calculations. Details are given in Refs. [49–51]. It should be mentioned that the analytical potential functions were constructed such as to describe more accurately the short-range rather than the long-range interactions.

Contours of the adiabatic PESs are depicted in Figs. 6(a) and 6(b), projected in the (R, γ) Jacobi coordinate plane. R is the distance of the sulfur atom from the center of mass of CO, and γ the angle between the CO bond length (r) and R; the $\gamma = 0$ degree corresponds to the OC-S nuclear configuration and $\gamma = 180$ degrees to S-OC. We denote with ξ the three Jacobi coordinates, $\xi = (R, r, \gamma)^T$ (the superscript [^{T}] denotes the column vector).

In Fig. 6 the CO bond is kept fixed at its equilibrium value, 2.2 bohr. In the middle part of the A surface [Fig. 6(b)], there is a local minimum at $\xi = (4.2$ bohr, 2.2 bohr, 48°) and an associated saddle index 1 at $\xi = (5.5$ bohr, 2.14 bohr, 46.7°). Similarly, a metastable minimum is present in the X surface [Fig. 6(a) at $\xi = (3.4$ bohr, 2.16 bohr, 85°) and a saddle index 2 at $\xi = (4.6$ bohr, 2.16 bohr, 86.5°).

The A surface is directly accessed by the photolysis laser, which transfers population from the (bend vibrationally excited) ground electronic X state. Most of the population proceeds to dissociation directly from this surface. Nevertheless, as has been shown in Ref. [37], part of the population is nonadiabatically transferred to the X state, which is responsible for the production of the highest rotational states of CO, $58 \leqslant J_{CO} \leqslant 66$ [52].

Comparing the resonant quantum states depicted in Fig. 6 here and the corresponding Fig. 3 in Ref. [37], we observe a more prominent nodal structure along the dissociation coordinate R for the currently examined photolysis energies of ~43 050 cm^{-1} [Fig. 6(b)] and ~43 400 cm^{-1} [Fig. 6(c)] in

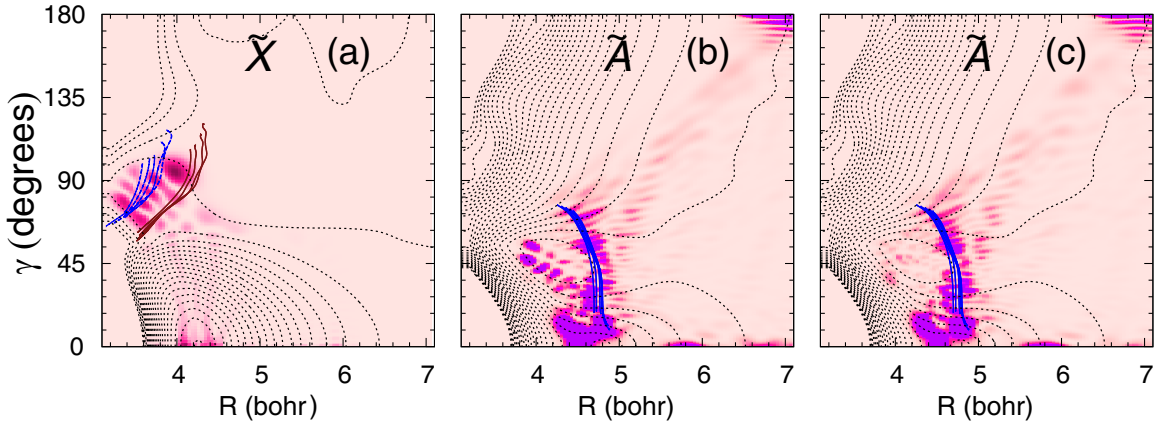

FIG. 6. (a) Contours and periodic orbits of the adiabatic X-PES for the ground electronic state projected in the (R, γ) Jacobi coordinate plane, with $r_{CO} = 2.2$ bohr. The energy ranges covered by the POs are (33 000–49 000) cm^{-1} (blue) and (35 000–48 000) cm^{-1} (brown). Overlaid is a resonant quantum state in the X-PES with energy 34 430 cm^{-1}. (b) Contours of the adiabatic PES for the A electronic excited state. In the same figure representative periodic orbits of the CSA1 family covering the energy range of 38 000–49 000 cm^{-1} are also shown. A resonant quantum state at 43 073 cm^{-1} (R_5) in the adiabatic A-PES is depicted. (c) Same as (b) but for a resonant state at 43 383 cm^{-1}, called R_6 in this work.

the A-PES. This new structure at internuclear distances larger than 5 bohr indicates a higher contribution from the continuous part of the wave function. This increased interaction supports the experimental findings shown in Fig. 5(d) and the dispersive shape of the "recoil resonance" in the photolysis area around 43 500 cm^{-1}.

B. Diabatic potential energy surfaces

Due to the presence of an avoided crossing between X-PES and A-PES, which was already pointed out by Suzuki *et al.* [53] and McBane *et al.* [52], realistic three-dimensional wave-packet propagations on the A state should include nonadiabatic transitions to the ground electronic state. These transitions are implemented in the nuclear quantum-mechanical equations by means of a diabatization procedure. Following a similar strategy to the one used for the fragmentation of H_2O^+ [54], a new set of diabatic states $(\Phi_X, \Phi_A)^T$ is obtained by means of a unitary transformation $\hat{U}$ of the adiabatic electronic states $(\Psi_X, \Psi_A)^T = \hat{U}(\Phi_X, \Phi_A)^T$. The new diabatic potentials given by the 2×2 matrix $\hat{V}^d$ are obtained by the linear transformation of the adiabatic $\hat{V}^a_{\mathrm{X(A)}}$ PESs:

$$\begin{pmatrix} V^d_{\mathrm{XX}} & V^d_{\mathrm{XA}} \\ V^d_{\mathrm{XA}} & V^d_{\mathrm{AA}} \end{pmatrix} = \hat{U}^\dagger \begin{pmatrix} V^a_X & 0 \\ 0 & V^a_A \end{pmatrix} \hat{U}, \tag{3}$$

where

$$\hat{U}(\xi) = \begin{pmatrix} \cos\Theta(\xi) & \sin\Theta(\xi) \\ -\sin\Theta(\xi) & \cos\Theta(\xi) \end{pmatrix}, \tag{4}$$

and Θ is the transformation angle of the diabatization. From the infinite number of possible transformations, we choose the one that minimizes the dynamical couplings along the nuclear coordinates ξ. The angle can thus be obtained from the expression [55]

$$\Theta(\xi) = \int_{\xi_0}^{\xi} \mathrm{d}\xi' \langle \Psi_X | \frac{\partial}{\partial \xi'} | \Psi_A \rangle, \tag{5}$$

where $\langle \Psi_X | \frac{\partial}{\partial \xi'} | \Psi_A \rangle$ denotes the nonadiabatic coupling vector (NACV). ξ_0 is chosen such as at the initial time the wave packet is on the A surface with negligible coupling to the X state. Similarly to N_2O, in the OCS molecule, motion along R and r yields dynamical couplings much smaller to those associated to the angular γ coordinate, and thus they can be neglected [52,53,56]. Moreover, due to the stiffness of CO bond, its internuclear distance r is kept fixed at 2.2 bohr along the nonadiabatic transitions. Apart from that, the dynamics are carried out in three-dimensional configuration space for both states. The integral $\langle \Psi_X | \frac{\partial}{\partial \gamma} | \Psi_A \rangle$ has been previously calculated by McBane *et al.* [52] using the MOLPRO program at the CASSCF level and with the aug-cc-pVTZ basis set.

C. Classical and quantum-mechanical calculations

Both classical and time-dependent quantum calculations have been carried out separately in the two adiabatic PESs. The classical calculations are used in the periodic orbit analysis for the detection of localized trajectories above the dissociation threshold in the pertinent PES. Theory and methodologies for locating periodic orbits as well as computing the continuation-bifurcation diagrams of their families by varying the period of POs have been described before [57,58]. This kind of classical mechanical analysis is based on semiclassical arguments which claim that time-invariant structures in phase space, such as tori and remnants of them, may identify quantum-mechanical eigenfunctions localized in the same regions of configuration space as the projections of periodic orbits [59].

Quantum molecular wave-packet propagations have been carried out using a grid-based parallel FORTRAN 95 code (grid-time-dependent Schrödinger equation (GTDSE) computational package [54,60]). The nuclear dynamics of the system are governed by the time-dependent Schrödinger equation, which for the specific case of total angular momentum $J = 0$

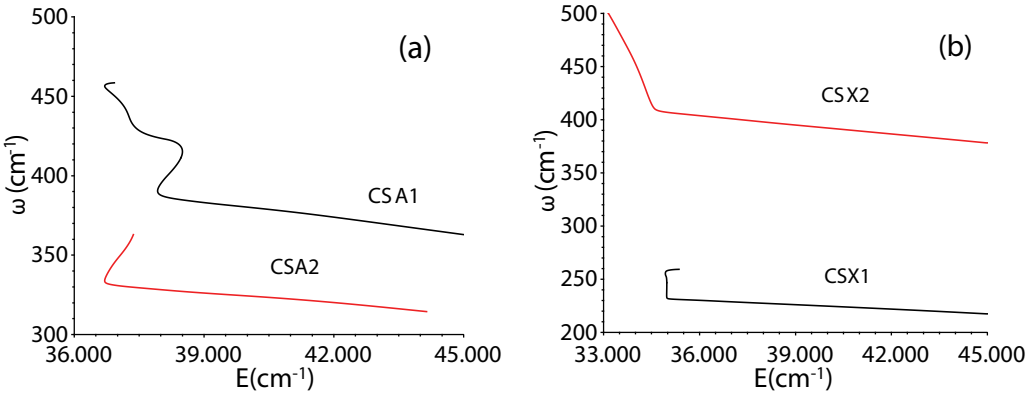

FIG. 7. Continuation-bifurcation diagrams projected in the energy-frequency plane for two families of periodic orbits in the X-PES (CSX1, CSX2) and A-PES (CSA1, CSA2), respectively.

reads as follows:

$$-\frac{\hbar^2}{2\mu_R R}\frac{\partial^2}{\partial R^2}[R\Psi(\xi,t)] - \frac{\hbar^2}{2\mu_r r}\frac{\partial^2}{\partial r^2}[r\Psi(\xi,t)] - \frac{\hbar^2}{2}\left(\frac{1}{\mu_R R^2}+\frac{1}{\mu_r r^2}\right)\left(\frac{\partial^2}{\partial\gamma^2}+\cot\gamma\frac{\partial}{\partial\gamma}\right)\Psi(\xi,t) + V(\xi)\Psi(\xi,t) = i\hbar\frac{\partial\Psi(\xi,t)}{\partial t}. \quad (6)$$

$\Psi(\xi,t)$ represents the total wave packet evolving in time.

The direct integration of Eq. (6) is achieved by means of finite difference algorithms, employing a grid of $N_R = 301$, $N_r = 50$, and $N_\gamma = 400$ points, respectively, for the $R \in [3, 15]$ bohr, $r \in [1.6, 3.6]$ bohr, and $\gamma \in [0, \pi]$ coordinates. The values of the wave function on the selected grid of $N_g = N_R \times N_r \times N_\gamma$ points are stored as a complex vector, while the Hamiltonian operator turns into a sparse $N_g \times N_g$ matrix, where the off-diagonal terms are the Fornberg coefficients used in the finite difference approximation to account for the derivatives in the Laplacian [58]. The diagonal part of the matrix is determined by the value of the potential energy.

Finally, the time evolution of the wave packet is carried out by means of a second-order difference scheme, which usually requires small time steps ($\Delta t = 5 \times 10^{-3}$ fs in the present calculations). The total integration time was up to 320 fs.

In order to prevent the reflection of the wave packet at the borders of the grid, as is characteristic of dissociative processes, the wave packet is absorbed through a Gaussian damping function [61,62] that is introduced at R_∞, before the limit R_L of the dissociative coordinate ($R_\infty = 12$ and $R_L = 15$ bohr).

The analysis of the rotational distribution in the time-dependent scheme is performed by Fourier transforming the coefficients $C_{vj}(t)$ given by the expression [63]

$$C_{vj}(t) = \int_0^\infty r^2 \mathrm{d}r \int_0^\pi \mathrm{d}\gamma \sin\gamma \left[\phi_{vj} Y_j^m(\gamma)\right]^* \Psi(R_\infty, r, \gamma, t), \quad (7)$$

as explained by Balint-Kurti *et al.* [64], where ϕ_{vj} are the CO rovibrational eigenfunctions and $Y_j^m(\gamma)$ the spherical harmonics.

Nonadiabatic effects are introduced in the quantum equations of motion by means of a previous diabatization procedure [54], employing the NACV between the A- and the X-PES. In the diabatic representation, the potential energy is not diagonal as in the adiabatic case, but instead, the off-diagonal element V_{XA}^d in Eq. (3) couples the evolution of the wave packet in both surfaces A and X. Nevertheless, the numerical scheme is almost identical to the one employed for a single adiabatic state, with the difference that the wave function has now two components (X and A) evolving simultaneously, coupled on the same nuclear configuration grid of points.

D. Results

Once the wave packet is transferred to the (excited) A surface by the photolysis field, it evolves in time in a nontrivial fashion. A periodic orbit analysis as well as quantum dynamical calculations in the adiabatic A-PES have revealed localized resonant eigenfunctions in the region of $R \approx 4.5$ bohr. In Figs. 6(b) and 6(c) we show representative periodic orbits localized towards the saddle index 1 of the A-PES. These unstable POs belong to the CSA1 family emanating from a center-saddle bifurcation [Fig. 7(a)].

In a Franck-Condon transition the initial wave packet $\Psi(\xi, 0)$ in the quantum calculations is prepared by taking the ground electronic-vibrational state multiplied by the transition dipole moment. It is projected in an area of the A-PES close to the linear configuration ($R = 4.2$ bohr, $\gamma \sim 7^\mathrm{o}$) of the OCS molecule. At later times, while most of the population dissociates in relatively small angles ($\gamma < 60^\mathrm{o}$), part of the wave packet is trapped near the local minimum of A-PES shown in Figs. 6(b) and 6(c).

The total photodissociation cross sections are computed from the Fourier transform of the autocorrelation function $C(t) = \langle\Psi(\xi,0)|\Psi(\xi,t)\rangle$ shown in Fig. 8 with the red line. The smooth curve with no peaks indicates that there are no recurrences of the wave packet to the initial region of configuration space. On the other hand, an initial Gaussian wave packet centered at $R = 4.6$ bohr produced a spectrum with peaks separated by $\sim$400 cm^{-1}, thus revealing resonances (black line).

We have extracted the wave functions, which correspond to the peaks $R_1 - R_6$ marked by the blue perpendicular lines in Fig. 8. In Figs. 6(b) and 6(c) we plot such resonant eigenstates alongside the periodic orbits. All extracted eigenfunctions

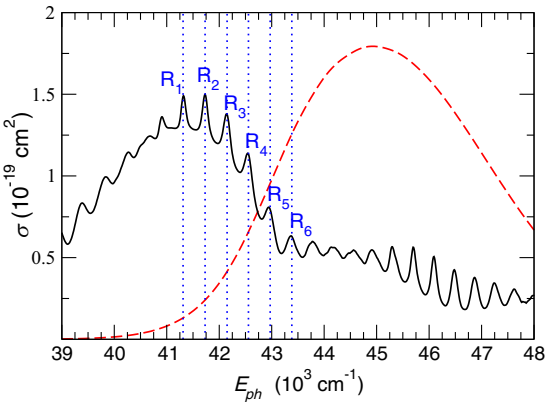

FIG. 8. Photodissociation cross sections calculated numerically from two different initial wave packets: the Franck-Condon initial wave packet (broken red line), centered at $R = 4.2$ bohr, $r = 2.2$ bohr, $\gamma = 7°$; and a Gaussian wave packet (solid black line) centered at $R = 4.6$ bohr, $r = 2.2$ bohr, $\gamma = 7°$. The resonances found for the latter are marked with vertical dotted blue lines at photolysis energies 41 350 cm^{-1} (R_1), 41 762 cm^{-1} (R_2), 42 150 cm^{-1} (R_3), 42 625 cm^{-1} (R_4), 43 073 cm^{-1} (R_5), and 43 383 cm^{-1} (R_6).

exhibit a nodal structure arranged along γ and small variation in R, thus demonstrating motion mainly along the angle.

The diffused character of the resonances R_5 and R_6 at 43 073 cm^{-1} and 43 383 cm^{-1}, respectively, compared to the prominent nodal pattern at 42 625 cm^{-1} (R_4, depicted in Fig. 3(b) of Ref. [37]), is the result of a higher contribution from the direct dissociating flux, which blurs the nodal structure. In fact, the intensity of the signal in Fig. 8 at both resonant peaks is lower for R_5 and R_6 than for R_4, which could explain why the effect on the recoil velocity distribution diminishes at high energies.

Most importantly, the resonances found in the excited electronic state are localized in that region of configuration space where nonadiabatic coupling to the X state is expected to be high [52,53]. Similar to the A state, classical and quantum calculations in the adiabatic X-PES unveil resonances, now localized at higher angles but at smaller R distances. Figure 6(a) depicts representative periodic orbits of two families originated from center-saddle bifurcations [Fig. 7(b)] and a resonant quantum state extracted from the GTDSE calculations. Notice that in these resonances sulfur bounces in the repulsive part of the potential, predicted at small R distances but larger angles with motion mainly along γ. Trajectories run from this region dissociate the sulfur atom from the oxygen side with high angular momentum. Hence, the observed highly excited J_{CO} states, as well as large and negative β_1 values in the experiment [37], are in accord to the mechanism that emerged from the calculations.

In a series of quantum-mechanical calculations with the Franck-Condon initial wave packet, separately on the A state and with the adiabatic surface, we determined the distributions of the J_{CO} values for the dissociated product CO molecule as is shown in Fig. 9 (blue dashed line). We see that only states up to 55 are produced. Contrary to that, nonadiabatic calculations gave a second band with $J_{CO} \in [56 - 69]$. In Fig. 9 we plot the contributions to each J_{CO} state from the two diabatic surfaces, as well as their sum (black smooth

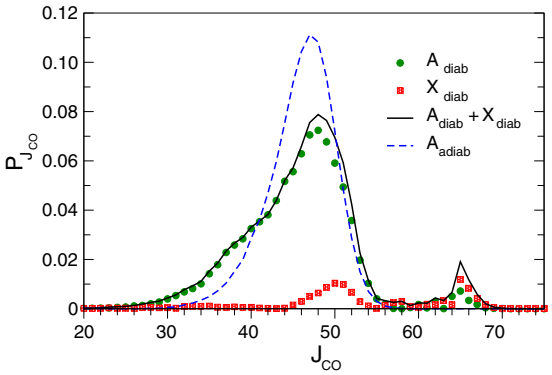

FIG. 9. Distribution of the J_{CO} product states in the dissociation of OCS on the A adiabatic surface is depicted with the dashed blue line. Contributions to each J_{CO} state from the two diabatic surfaces, as well as their sum (black smooth curve), are also presented from the nonadiabatic calculations.

curve). These quantum results are in accord with the classical surface-hopping calculations of McBane *et al.* [52]. In the Supplemental Material we include a video with the motion of the wave packet on both surfaces at the adiabatic representation [65]. A favorable comparison with the experimental relative intensities has been found and presented in Ref. [37], Fig. 4.

The appearance of the two bands in the J_{CO} distributions, one covering the range of $34 \leqslant J_{CO} \leqslant 54$ and the second $59 \leqslant J_{CO} \leqslant 69$, calls for further investigation. In Fig. 10 we show the time evolution of the square of the overlap integral between the excited Franck-Condon wave packet from the ground to the upper surface and the six resonance eigenfunctions examined in the A state. Single adiabatic state calculations demonstrate that the overlap integral remains almost constant between 10 and 150 fs and is zero after 170 fs (red lines). In contrast, we do find population transfer to the ground electronic state in the nonadiabatic calculations. The dip shown in the blue curves of Fig. 10, in the time interval of 50–100 fs, occurs in coincidence with the increase of the overlap integral in the ground state (black curves) and unveils a reflection of the wave packet from the ground back to the excited state.

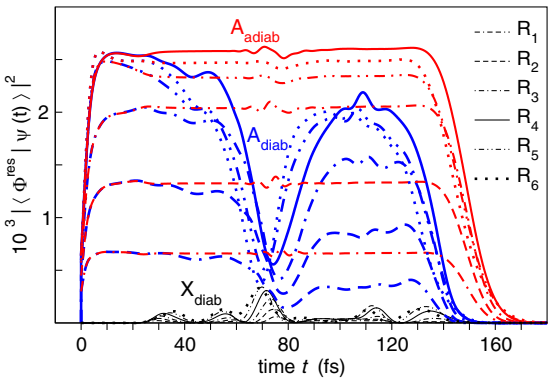

FIG. 10. Time evolution of the squared overlap integral between the excited wave packet and the resonance wave functions ($R_1 - R_6$) of the A state for both diabatic and adiabatic calculations.

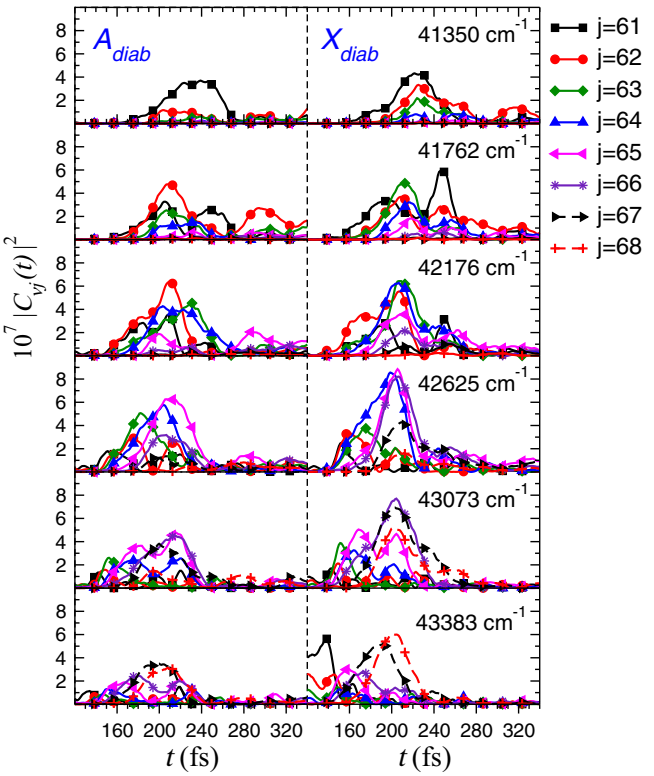

FIG. 11. Squared overlap integral of the evolving excitation wave packet in the A and X states with the product states $J_{CO} =$ 61–68 wave functions in the nonadiabatic calculations.

In association with this, Fig. 11 depicts the time evolution of the overlap integrals of the evolving wave packet with the high $J_{CO} = 61 - 68$ product states. These states start gaining intensity only after the elapse of ∼150 fs, a time which coincides with the diminishing of the overlap of the wave packet with the resonance states (Fig. 10). In Fig. 10 we underline the increasing overlap with the energy of the resonance states, reaching its maximum at R_4 (42 625 cm^{-1}) and then decreasing again, as is deduced from the intensity of the highest studied resonance.

IV. DISCUSSION AND CONCLUSION

Resonantlike variations in the recoil velocity distribution are identified at energies around 42 700 and 43 500 cm^{-1}, which indicates that a family of resonances exists which affects the high-J_{CO} states.

Nonadiabatic time-dependent quantum-mechanical calculations have been used to extract resonant states in the same energy range as the experimental one and were found to be localized in regions of nuclear configuration space previously identified by a periodic orbit analysis. These calculations show that population is trapped above shallow local minima in the two involved adiabatic PESs, the X and A states, coupled by nonadiabatic matrix elements with a major contribution from the angular derivative of the electronic wave function. Nonadiabatic transitions from the excited to the ground state lead to population exchange, which results in high torques exerted on the CO fragment, and thus to the production of the highest rotational states, $58 \leqslant J_{CO} \leqslant 69$, a result which is in agreement with classical, surface-hopping calculations reported in Ref. [52].

These highly excited rotational states are generated much later than all the lower rotational states, around 160–250 fs, thus revealing their associations with the resonance states. The localized quantum resonances along the angular degree of freedom and the production of high-J_{CO} states in relatively short times (150 fs) support dissociation dynamics where the sulfur atom leaves the triatomic molecule from the oxygen side of CO and thus the recoil inversion observed in [37].

A major difference between the dissociation dynamics observed in the two different areas of photolysis energies, namely, around 42 700 cm^{-1} and around 43 500 cm^{-1}, is the existence of increased interaction of the discrete and the continuous parts of the wave function. This results in different spectral shapes for the "recoil resonance," which resembles a Fano-type resonance [42] in the latter case.

In the experimental study, we can monitor the dissociation dynamics for several rotational states of the CO fragment and thus gain insights into how the dissociation proceeds for fragments of different kinetic energy. We expect that fragments of reduced kinetic energy are largely affected by the resonances present in the A-PES, while the fragments of higher kinetic energy not so, thus presenting a picture of the dissociation process in the absence of the resonant states discussed here. The study reveals that for photolysis energy around 42 700 cm^{-1}, and for the high-kinetic-energy fragments, the recoil geometry does not depend on small variations of the photolysis energy, while in the area of 43 500 cm^{-1} the recoil distributions become increasingly parallel to the polarization of the photolysis laser as its frequency increases.

The interaction of this slowly varying background with the resonant feature of the wave function indicates that a dispersive shape of the "recoil resonance" should be expected. Such variations in the observables of the experiments are indicative of the richness of these stereodynamic effects, which might be common in near-threshold dissociation experiments but might manifest themselves very differently in different photolysis energies and/or molecular systems.

The resonant eigenstates in the A state have been identified by families of POs emanating from center-saddle bifurcations named CSA1 and CSA2 in Fig. 7. These periodic orbits show that the frequencies exhibit a linear dependence with the energy. Semiclassically, these frequencies correspond to the energy difference between adjacent quantum levels and are estimated at ∼370 cm^{-1}, in good agreement with the resonance energies deduced from the experiment.

We emphasize that these types of resonances occur at several energies and not just at one specific energy. This is very important for demonstrating the effectiveness of nonlinear resonances, which are ubiquitous in excited small molecules. In the present article we have systematically investigated how the nonlinear resonances located in the adiabatic potential energy surfaces are perturbed by the nonadiabatic coupling elements. Conical intersections are not rare events at all, even in small polyatomic molecules. Hence, nonlinearity and nonadiabatic couplings may dramatically change the dynamics of the molecule and produce new physics and chemistry.

Nevertheless, as both are local effects (in configuration space as well as in phase space), this may result in diverse dynamical behaviors for different molecules [57].

ACKNOWLEDGMENTS

This research has been financially supported by the division of Chemical Sciences of the Netherlands Organization for Scientific Research (NWO). D.S. acknowledges support by the EC's Seventh Framework Program via the Marie Curie Initial Training Network ICONIC. D.S. and T.P.R. also acknowledge support by the project "HELLAS-CH" (MIS 5002735), which is implemented under the "Action for Strengthening Research and Innovation Infrastructures," funded by the Operational Program "Competitiveness, Entrepreneurship and Innovation" (NSRF 2014-2020) and cofinanced by Greece and the European Union (European Regional Development Fund). J.S. acknowledges support from the Laserlab-Europe through Grant No. ULF-FORTH002179. J.A.S. acknowledges funding from a Carlsberg Foundation postdoctoral fellowship (CF14-0519). J.S. thanks George McBane for providing the nonadiabatic coupling elements. D.S. thanks George McBane and Luis Rubio-Lago for useful discussions.

[1] R. Schinke, *Photodissociation Dynamics* (Cambridge University Press, Cambridge, UK, 1993).
[2] F. F. Crim, J. Phys. Chem. **100**, 12725 (1996).
[3] A. Assion, T. Baumert, M. Bergt, T. Brixner, B. Kiefer, V. Seyfried, M. Strehle, and G. Gerber, Science **282**, 919 (1998).
[4] T. Röckmann, M. E. Popa, M. C. Krol, and M. E. G. Hofmann, Sci. Rep. **6**, 31947 (2016).
[5] M. S. Johnson, G. D. Billing, A. Gruodis, and M. H. M. Janssen, J. Phys. Chem. A **105**, 8672 (2001).
[6] C. Brühl, J. Lelieveld, P. J. Crutzen, and H. Tost, Atmos. Chem. Phys. **12**, 1239 (2012).
[7] N. Glatthor, M. Höpfner, A. Leyser, G. P. Stiller, T. von Clarmann, U. Grabowski, S. Kellmann, A. Linden, B.-M. Sinnhuber, G. Krysztofiak *et al.*, Atmos. Chem. Phys. **17**, 2631 (2017).
[8] COS-OCS project website, http://cos-ocs.eu.
[9] D. W. Chandler and P. L. Houston, J. Chem. Phys. **87**, 1445 (1987).
[10] A. T. J. B. Eppink and D. H. Parker, Rev. Sci. Instrum. **68**, 3477 (1997).
[11] M. M. R. Fanood, N. B. Ram, C. S. Lehmann, I. Powis, and M. H. M. Janssen, Nat. Commun. **6**, 7511 (2015).
[12] J. Ullrich, R. Moshammer, A. Dorn, R. Dörner, L. P. H. Schmidt, and H. Schmidt-Böcking, Rep. Prog. Phys. **66**, 1463 (2003).
[13] X. Yang, Phys. Chem. Chem. Phys. **13**, 8112 (2011).
[14] D. W. Chandler, J. Chem. Phys. **132**, 110901 (2010).
[15] B. C. Shepler, Y. Han, and J. M. Bowman, J. Phys. Chem. Lett. **2**, 834 (2011).
[16] F. A. L. Mauguière, S. C. Farantos, J. Suarez, and R. Schinke, J. Chem. Phys. **134**, 244302 (2011).
[17] M. N. R. Ashfold, B. Cronin, A. L. Devine, R. N. Dixon, and M. G. D. Nix, Science **312**, 1637 (2006).
[18] D. Townsend, S. A. Lahankar, S. K. Lee, S. D. Chambreau, A. G. Suits, X. Zhang, J. Rheinecker, L. B. Harding, and J. M. Bowman, Science **306**, 1158 (2004).
[19] B. R. Heazlewood, M. J. T. Jordan, S. H. Kable, T. M. Selby, D. L. Osborn, B. C. Shepler, B. J. Braams, and J. M. Bowman, Proc. Natl. Acad. Sci. U. S. A. **105**, 12719 (2008).
[20] R. Sivaramakrishnan, J. Michael, A. Wagner, R. Dawes, A. Jasper, L. Harding, Y. Georgievskii, and S. Klippenstein, Combust. Flame **158**, 618 (2011).
[21] M. P. Grubb, M. L. Warter, H. Xiao, S. Maeda, K. Morokuma, and S. W. North, Science **335**, 1075 (2012).
[22] L. Poisson, D. Nandi, B. Soep, M. Hochlaf, M. Boggio-Pasqua, and J.-M. Mestdagh, Phys. Chem. Chem. Phys. **16**, 581 (2014).
[23] F. A. L. Mauguiére, P. Collins, B. K. Carpenter, G. S. Ezra, S. C. Farantos, and S. Wiggins, Annu. Rev. Phys. Chem. **68**, 499 (2017).
[24] T. P. Rakitzis, S. A. Kandel, A. J. Alexander, Z. H. Kim, and R. N. Zare, Science **281**, 1346 (1998).
[25] T. P. Rakitzis, P. C. Samartzis, and T. N. Kitsopoulos, J. Chem. Phys. **111**, 10415 (1999).
[26] Z. H. Kim, A. J. Alexander, and R. N. Zare, J. Phys. Chem. A **103**, 10144 (1999).
[27] A. G. Suits and O. S. Vasyutinskii, Chem. Rev. **108**, 3706 (2008).
[28] V. V. Kuznetsov, P. S. Shternin, and O. S. Vasyutinskii, Phys. Scr. **80**, 048107 (2009).
[29] R. N. Zare, IEEE **51**, 173 (1963).
[30] M. H. M. Janssen, J. W. G. Mastenbroek, and S. Stolte, J. Phys. Chem. A **101**, 7605 (1997).
[31] S. E. Choi and R. B. Bernstein, J. Chem. Phys. **85**, 150 (1986).
[32] R. N. Zare, Chem. Phys. Lett. **156**, 1 (1989).
[33] T. P. Rakitzis, A. J. van den Brom, and M. H. M. Janssen, Chem. Phys. Lett. **372**, 187 (2003).
[34] L. D. A. Siebbeles, M. Glass-Maujean, O. S. Vasyutinskii, and O. R. J. A. Beswick, J. Chem. Phys. **100**, 3610 (1994).
[35] R. N. Zare, *Angular Momentum: Understanding Spatial Aspects in Chemistry and Physics* (Wiley, New York, 1998).
[36] T. Seideman, Chem. Phys. Lett. **253**, 279 (1996).
[37] D. Sofikitis, J. Suarez, J. A. Schmidt, T. P. Rakitzis, S. C. Farantos, and M. H. M. Janssen, Phys. Rev. Lett. **118**, 253001 (2017).
[38] J. Jankunas, K. Jachymski, M. Hapka, and A. Osterwalder, J. Chem. Phys. **142**, 164305 (2015).
[39] A. Bergeat, J. Onvlee, C. Naulin, A. van der Avoird, and A. Costes, Nat. Chem. **7**, 349 (2015).
[40] Z. Gao, T. Karman, S. N. Vogels, M. Besemer, A. van der Avoird, G. C. Groenenboom, and S. Y. T. van de Meerakker, Nat. Chem. **10**, 469 (2018).
[41] S. N. Vogels, T. Karman, J. Kłos, M. Besemer, J. Onvlee, A. van der Avoird, G. C. Groenenboom, and S. Y. T. van de Meerakker, Nat. Chem. **10**, 435 (2018).

[42] U. Fano, Phys. Rev. **124**, 1866 (1961).
[43] M. L. Lipciuc, A. J. van den Brom, L. Dinu, and M. H. M. Janssen, Rev. Sci. Instrum. **76**, 123103 (2005).
[44] M. L. Lipciuc and M. H. M. Janssen, Phys. Chem. Chem. Phys. **8**, 3007 (2006).
[45] M. Brouard, A. V. Green, F. Quadrini, and C. Vallance, J. Chem. Phys. **127**, 084304 (2007).
[46] F. J. Lovas and P. H. Krupenie, J. Phys. Chem. Ref. Data **3**, 245 (1974).
[47] S. Hattori, S. O. Danielache, M. S. Johnson, J. A. Schmidt, H. G. Kjaergaard, S. Toyoda, Y. Ueno, and N. Yoshida, Atmos. Chem. Phys. **11**, 10293 (2011).
[48] B. W. Toulson and C. Murray, J. Phys. Chem. A **120**, 6745 (2016).
[49] J. A. Schmidt, M. S. Johnson, G. C. McBane, and R. Schinke, J. Chem. Phys. **136**, 131101 (2012).
[50] J. A. Schmidt, M. S. Johnson, G. C. McBane, and R. Schinke, J. Chem. Phys. **137**, 054313 (2012).
[51] J. A. Schmidt and J. M. H. Olsen, J. Chem. Phys. **141**, 184310 (2014).
[52] G. C. McBane, J. A. Schmidt, M. S. Johnson, and R. Schinke, J. Chem. Phys. **138**, 094314 (2013).
[53] T. Suzuki, H. Katayanagi, S. Nanbu, and M. Aoyagi, J. Chem. Phys. **109**, 5778 (1998).
[54] J. Suarez, L. Mendez, and I. Rabadan, J. Chem. Phys. Lett. **6**, 72 (2015).
[55] J. P. Malhado, M. J. Bearpark, and J. T. Hynes, Front. Chem. **2**, 1 (2014).
[56] G. C. McBane and R. Schinke, J. Chem. Phys. **136**, 044314 (2012).
[57] S. C. Farantos, R. Schinke, H. Guo, and M. Joyeux, Chem. Rev. **109**, 4248 (2009).
[58] S. C. Farantos, *Nonlinear Hamiltonian Mechanics Applied to Molecular Dynamics: Theory and Computational Methods for Understanding Molecular Spectroscopy and Chemical Reactions* (Springer, New York, 2014).
[59] S. C. Farantos, Phil. Trans. R. Soc. A **376**, 20170148 (2018).
[60] J. Suarez, S. C. Farantos, S. Stamatiadis, and L. Lathouwers, Comput. Phys. Comm. **180**, 2025 (2009).
[61] D. Dundas, J. F. McCann, J. S. Parker, and K. T. Taylor, J. Phys. B **33**, 3261 (2000).
[62] D. Manolopoulos, J. Chem. Phys. **117**, 9552 (2002).
[63] J. A. Schmidt, M. S. Johnson, U. Lorenz, G. C. McBane, and R. Schinke, J. Chem. Phys. **135**, 024311 (2011).
[64] G. G. Balint-Kurti, R. N. Dixon, and C. C. Marston, J. Chem. Soc., Faraday Trans. **86**, 1741 (1990).
[65] See Supplemental Material at http://link.aps.org/supplemental/10.1103/PhysRevA.98.033417 for a video showing the motion of the wave packet on both surfaces at the adiabatic representation.